nature microbiology

SUPPLEMENTARY INFORMATION

https://doi.org/10.1038/s41564-020-0686-0

In the format provided by the authors and unedited.

Genetically engineered control of phenotypic structure in microbial colonies

Philip Bittihn[1,2,5], Andriy Didovyk[1,6], Lev S. Tsimring[1,2] ✉ and Jeff Hasty[1,2,3,4] ✉

[1]BioCircuits Institute, University of California, San Diego, La Jolla, CA, USA. [2]The San Diego Center for Systems Biology, La Jolla, CA, USA. [3]Department of Bioengineering, University of California, San Diego, La Jolla, CA, USA. [4]Molecular Biology Section, Division of Biological Sciences, University of California, San Diego, La Jolla, CA, USA. [5]Present address: Max Planck Institute for Dynamics and Self-Organization, Göttingen, Germany. [6]Present address: Vertex Pharmaceuticals, San Diego, CA, USA. ✉e-mail: ltsimring@ucsd.edu; hasty@bioeng.ucsd.edu

Supplementary Information

Genetically engineered control of phenotypic structure in microbial colonies

Philip Bittihn,[1,2,3] Andriy Didovyk,[1,4] Lev S. Tsimring,[1,2,†] and Jeff Hasty[1,2,5,6,†]

[1] *BioCircuits Institute, University of California, San Diego, La Jolla, California, USA*

[2] *The San Diego Center for Systems Biology, La Jolla, California, USA*

[3] *Current address: Max Planck Institute for Dynamics and Self-Organization, Göttingen, Germany*

[4] *Current address: Vertex Pharmaceuticals, San Diego, California, USA*

[5] *Department of Bioengineering, University of California, San Diego, La Jolla, California, USA*

[6] *Molecular Biology Section, Division of Biological Sciences, University of California, San Diego, La Jolla, California, USA*

[†] Email: ltsimring@ucsd.edu, hasty@bioeng.ucsd.edu

Supplementary Discussion

1 Unsuccessful phenotype elimination using standard pLuxI promoter

Our first attempt to eliminate the growth-arrested phenotype from the population, before the construction of the gating module, was to take advantage of the non-dividing cells' capacity for protein expression and degradation (Figs. 1g, h) using our standard, bidirectional, AHL-inducible pLuxI expression cassette (identical to that used for RFP-ssrA; Fig. 1h), as it appeared to support strong expression and had a natural preference for the dormant cells. In this cassette, LuxR is constitutively expressed from its native pLuxR promoter (Supp. Fig. 4). However, when we placed ssrA-AAV-tagged lysis protein E under the control of this standard pLuxI expression cassette and the construct was activated in the microcolonies with sufficient AHL, dividing cells began lysing first, causing dormant cells to start regrowing before also lysing (Extended Data Fig. 7a; Supplementary Movie 5). After regrowth, the colonies eventually settled into a disorganized state of constant partial lysis for all effective AHL concentrations (Extended Data Fig. 7b, c), without any visible phenotype elimination. The fact that growth in these final steady-states could be observed *deeper* in the trap than without lysis (compare different end states to 0 nM in Extended Data Fig. 7c), indicated that the expression of the lysis protein continuously affects the growth pattern of *dividing* cells, either creating "holes" or slowing down growth, and thus allowing nutrients to diffuse deeper into the trap. In addition, we still observed dormant cells in the back of the trap, seemingly unaffected by lysis. These could be descendants of previously dividing cells in which

mutations deactivated the lysis module due to the immense selective pressure. Alternatively, they indicate insufficient expression of lysis protein. All of these problems seemed to point to one common root cause: the expression level of lysis protein E from the standard pLuxI promoter was too high in dividing cells compared to growth-arrested cells. This motivated the construction of the gating module that would shift expression towards the non-dividing phenotype.

2 Numerical Modeling

Our model of the full sensor-actuator circuit describes the coupled dynamics of the cellular concentration of the growth repression *protein p* expressed from the sensor promoter, and the *capacity* c of the cell to activate the stress-responsive sensor promoter. In a single cell, the model equations are

$$\dot{p} = \beta \cdot P(f,c) - \gamma_p \cdot p - g(f,p) \cdot p \tag{1a}$$

$$\dot{c} = C(f,p) - \gamma_c \cdot c - g(f,p) \cdot c \tag{1b}$$

with

$$P(f,c) = \sigma + c \cdot \exp\left(-F_1 \cdot (f - f_{crit})^2\right) \tag{2}$$

$$C(f,p) = g(f,p). \tag{3}$$

denoting synthesis and degradation rates for the corresponding components that depend on their own concentrations and the concentration of the critical nutrient concentration ("food") f. By choosing sufficiently large $F_1 \gg 1$ we enforce that the growth repression protein (GRP) is expressed from the stress-activated sensor promoter only when f is near a specific (low) value of $f = f_{crit}$ ("metabolic stress") proportional to the cell's stress response capacity c. Note that, while the small leaky expression rate of the stress sensor resulting from σ is generically assumed to be present, it can be set to 0 in the context of the sensor and actuator dynamics without changing any results shown in this study. It only becomes relevant in the context of the gating circuit (see corresponding section below). Otherwise, the synthesis rate is proportional effective promoter strength of the sensor $\beta = \beta_{metabolic} + \mathrm{NaCl}$, where $\beta_{metabolic}$ is the fixed promoter strength in the absence

of additional NaCl in the growth medium (which can be seen, e.g., in Extended Data Fig. 1f), and NaCl represents the variable increase in expression level resulting from increased osmolarity (Fig. 1e). As the proteins that we express from the sensor promoter are ssrA-tagged and ClpXP is active in stationary phase in batch as well as non-growing cells in microfluidics (cf. Figs. 1e and 1h), p has an intrinsic degradation rate γ_p.

In addition to synthesis and degradation, both p and c are also diluted with a rate that is equal to the cellular growth rate $g(f,p)$, reflected by the second terms in the r.h.s. of both Eqs. (1). The stress response capacity c represents the ability of the cell to elicit a stress response due to food scarcity. At any given instant, it tends towards a value of $g(f,p)/[\gamma_c + g(f,p)])$. Its nominal (maximum) value in growing cells is therefore $g_0/(\gamma_c + g_0)$. When a cell stops growing ($g(f,p) = 0$), its level of c decays exponentially with rate γ_c towards zero. After growth resumption, the capacity c first has to recover sufficiently for cells to activate the sensor promoter in response to nutrient stress, as suggested by the lack of an immediate stress response in non-dividing cells close to the no-growth boundary (Extended Data Fig. 3a) and cells that have just resumed growth (Fig. 2f).

The growth rate itself depends on the nutrient concentration f and the amount of GRP p,

$$g(f,p) = g_0 \cdot \max\{0, \tanh[F_2 \cdot (f - f_{crit})]\} \cdot \max\left\{0, 1 - (p/p_{crit})^3\right\}, \tag{4}$$

where g_0 is the maximum growth rate. The first $\max\{...\}$ term on the right hand side models the sharp (we choose $F_2 \gg 1$) growth rate dependence on the food concentration near the critical

food concentration f_{crit} where it drops to zero. The second $\max\{...\}$ term models the reduction in growth rate by the growth repression protein, reaching 0 for a critical value p_{crit}.

The dynamics of the nutrient concentration f depends on the specific experimental setup: For example, in batch culture, it is depleted from initial concentration f_0 with the rate proportional to the cell density n and the per-cell nutrient consumption rate $F(f,p)$

$$\dot{f} = n \cdot F(f,p) = -n \cdot \max\{\alpha \cdot g(f,p), \alpha_0\} \tag{5}$$

This expression indicates that f is consumed with a rate that is proportional to the growth rate g, but never falls below a basal metabolic turnover rate α_0 even if cells do not grow.

Equations (1) – (5) represent the basal model of the sensor-actuator circuit.

Decoupling sensor and actuator components

We decouple the sensor (promoter) and actuator (growth repression protein, GRP) components in the above model in order to compare them separately to the experiments of the isolated sensor and actuator modules. Modeling of the sensor module (Fig. 1d) is straightforward, as all the induction characteristics of p are preserved. However, since p in this case is simply GFP-ssrA (without the growth-modulating effect of GRP), we exclude its effect on the growth rate and replace Eq. (4) by

$$g^*(f) = g_0 \cdot \max\{0, \tanh(F_2 \cdot (f - f_{crit}))\}. \tag{6}$$

We then interpret p simply as the fluorescence without any feedback on cell growth.

To model the isolated actuator module (with IPTG-controlled induction of GRP, Fig. 2a), we replace Eq. (2) in Eq. (1a) for the growth repression protein p with

$$P^*(f,p,c) = P^*(f,p) = \mathrm{IPTG} \cdot \max\{\delta, \tanh(F_2 \cdot (f - f_{crit}))\}, \tag{7}$$

which decouples it from the cell's stress response (c is irrelevant in this context). In this case, we assume that the synthesis of GRP is proportional to the concentration of IPTG and the instantaneous growth rate $g^*(f)$, however below f_{crit} it remains small but finite ($\delta \ll 1$), in accordance with microfluidic experiments that show a much-weakened response in non-growing cells, even though dilution is completely absent (Fig. 2b). The residual production rate is required to account for the fact that GRP levels remain high even in stationary phase despite being ssrA-tagged (Fig. 2a) and that for high enough induction, expression can eventually be detected in non-growing cells (cf. Fig. 2b and Extended Data Fig. 4d).

Batch culture model

In batch culture, the cell density n grows with the instantaneous growth rate $g(f,p)$:

$$\dot{n} = g(f,p) \cdot n \tag{8}$$

To model the dynamics of the sensor module in the batch culture, we integrate the basal model, Eqs. (1), (5), together with this equation for the cell density, where we replace g with g^* from Eq. (6). Numerical simulations lead to the temporal dynamics shown in Extended Data Fig. 5a. Similarly, to model the batch culture experiment with the isolated actuator module induced by IPTG, we integrate the basal model and the cell density equation with P replaced by P^*, Eq. (7).

Extended Data Figure 5b shows the results of this simulation for three values of the IPTG concentration. Both of these numerical simulations closely match experimental observations shown in Figs. 1e and Fig. 2a.

Gating circuit model

To model the gating circuit, we extend our previously developed model of lysis protein expression from the pLuxI promoter[1] by accounting for different growth phases and the expression of LuxR consitutively (ungated case) or from the stress promoter pOsmY (gated case). The ungated expression of the target gene from the pLuxI promoter is modeled by coupled equations for constitutive expression and dilution of LuxR,

$$\dot{l}_R = L_0 \cdot \hat{g}(f) - g(f,p) \cdot l_R \tag{9}$$

and the inducible expression, enzymatic degradation and dilution of the target protein R,

$$\dot{R} = \beta_R \cdot \hat{g}(f) \cdot G(A \cdot l_R) - g(f,p) \cdot R - \gamma_R(1 + \alpha_R g(f,p)) \tag{10}$$

Here $G(q) = \alpha_q + \alpha_q^* q^z/(q_c^z + q^z)$ is the Hill function describing activation of the pLuxI promoter by the complex of LuxR and AHL, and A is the concentration of AHL. In both equations (9) and (10), we multiply the production rates by the function $\hat{g}(f) = \tanh(50f)$, which prevents protein production from continuing indefinitely at high levels deep into stationary phase. Expression deep in stationary phase, while still present (cf. Fig. 1), is significantly weaker overall than in exponential phase. This is also confirmed by the fact that the experimental RFP curves in Extended Data Figs. 8a display a clear maximum after the cells enter stationary phase. To mimic this behavior, we

stop protein production when f reaches 0 due to the residual metabolism in Eq. (5) (we could have implemented a small residual expression rate later in stationary phase as in Eq. (7), which would, however, not change the results).

The term $\gamma_R(1+\alpha_R g(f,p))\cdot R$ describes enzymatic degradation of ssrA-tagged RFP which is stronger in growing cells and weaker, but still non-zero, in non-growing cells[2]. These equations have to be solved together with the basic model Eqs. (1)-(5).

In the gating module (cf. Fig. 3b), LuxR protein synthesis is driven by the stress-induced promoter pOsmY, so equation (9) is replaced by

$$\dot{l}_R = \beta_l P(f,c) - g(f,p)\cdot l_R \tag{11}$$

with the induction function $P(f,c)$ taken from (2).

Extended Data Figure 9a,b show the time courses of the target protein R (RFP) for ungated and gated cases for $A = 100$. Extended Data Figure 9c shows the gating fidelity of target gene expression that is defined as the ratio of the peak induction level $\max(R(t))$ to the value of R when $n = 7\cdot 10^{-4}$ ($OD = 0.7$), similar to the experiment. Note that, in order to achieve the decline of the gating fidelity in the gated circuit towards higher inducer levels, leaky expression from the stress sensor (σ in $P(f,c)$, eqs. (2), (11)) is strictly necessary. For $\sigma = 0$, no LuxR would be present during exponential phase, fixing RFP induction level at the basal expression level from the pLuxI promoter ($G(0)$ in Eq. (10)) for all AHL concentrations A, leading to a monotonic increase in gating fidelity as A increases the peak induction level. In contrast, $\sigma > 0$ enables large A to also increase

RFP expression during exponential phase (due to the presence of a small amount of LuxR), leading to a decline of the gating fidelity when exponential phase induction starts increasing more rapidly than peak RFP induction (as in the experiment, Fig. 3c).

To model the dynamics of gated or ungated lysis circuit, we add the effect of the target protein concentration R (which is the lysis protein in this case) to equation (8) for the cell density n,

$$\dot{n} = \max\{g(f,p) - \gamma_n^* R, 0\} \cdot n - \gamma_n \max\{R - R_0, 0\} \cdot n \tag{12}$$

The two terms represent the detrimental effect of R on the exponential growth rate at low concentrations (first term) and the actual lysis of cells at high concentrations (second term). This is necessary, since, according to Fig. 3, cells can tolerate levels of lysis protein during stationary phase resulting from the basal expression levels of pLuxI (in the absence of AHL). Moreover, in the ungated circuit, killing during stationary phase becomes effective at the same AHL levels that also impact growth (Fig. 3e), despite a gating fidelity of about 10 (Fig. 3c), which indicates that lysis protein levels after entering stationary phase should be about 10 times as high as during exponential phase. This is only possible if the protein levels that impact growth rate are significantly lower than those inducing killing.

Extended Data Figure 9d,e show the time courses of OD and the concentration of the lysis protein R at different values of AHL concentration A for ungated (d) and gated (e) cases.

In our simulations, we used the following additional parameters for the gating circuit: $L_0 = 0.2, \beta_l = 10, \alpha_R = 10/g_0, \gamma_R = 0.5, \beta_R = 20, \alpha_q = 0.03, \alpha_q^* = 1, z = 1, q_c = 100, \gamma_n = 0.2, \gamma_n^* = 1, R_0 = 5$.

Spatiotemporal model

To model the populations of cells harboring the sensor and actuator modules in the spatial context of a microfluidic trap, we construct a one-dimensional reaction-diffusion-advection model that generalizes the intra-cellular basal model (1) and the food equation (5), where p, c and f become fields over a spatial coordinate x. $x = 0$ corresponds to the mouth of the trap and $x = L$ corresponds to the back wall. For simplicity, we assume a constant cell density throughout the trap, eliminating the need for an explicit dynamic variable n (we set $n = n_{trap}$ everywhere, see "Parameters" section for details). We impose Dirichlet boundary condition $f(0) = f_0$ at $x = 0$ to model fresh media supply at the mouth of the trap, and no-flux boundary conditions for all variables at $x = L$. Extracellular $f(x,t)$ is only subject to diffusion with diffusion constant D_f, whereas $p(x,t)$ and $c(x,t)$ are intracellular quantities which are not diffused, but advected through the trap due to cell motion caused by growth. Assuming that cells in the microfluidic trap are densely packed and incompressible, the velocity $v(x,t)$ is determined by the instantaneous, cumulative cell growth rate in the trap

$$v(x,t) = \int_L^x g(f(x,t), p(x,t))\,\mathrm{d}x, \tag{13}$$

(the velocity is always zero at the back wall $x = L$). Note that this velocity field is *not* divergence-free due to local growth. This also means that dilution of p and c is already implicitly modeled through advection (which is consistent since the divergence of the velocity field $\frac{\partial v}{\partial x}$ is exactly

$g(f,p)$). Hence, the full system of partial differential equations is

$$\frac{\partial p}{\partial t} = P(f,p,c) - \frac{\partial (pv)}{\partial x} \tag{14a}$$

$$\frac{\partial c}{\partial t} = C(f,p,c) - \frac{\partial (cv)}{\partial x} \tag{14b}$$

$$\frac{\partial f}{\partial t} = n_{trap} \cdot F(f,p) + D_f \frac{\partial^2 f}{\partial x^2} \tag{14c}$$

We simulated this system of advection-reaction-diffusion equations using implicit finite difference first-order in time and second-order in space integrator in MATLAB™ using the same parameter values as for batch culture simulations. Numerical simulations of this system with the actuator modification, Eq. (7), lead to Extended Data Fig. 5c, reproducing the experimental observation of growth resumption in Fig. 2b and Extended Data Fig. 4d, e. Simulations of the full system of equations without modifications produced Figs. 2d, e and Extended Data Figs. 5d, e.

Parameters and initial conditions

To make sure that our batch culture and spatiotemporal simulations are consistent with each other, and that the physical scales of growth and nutrient consumption/transport are realistic, we chose them accroding to the following strategy: The growth rate was taken directly from plate reader experiments (e.g., Supp. Fig. 3). For the cell density n, we assumed natural, dimensionless units of the fractional volume occupied by cells. In these units, an OD600 of 1 corresponds to approximately $n = 0.1\%$ or 10^{-3} according to the literature[3]. We arbitrarily chose $f_0 = 1$ as the initial nutrient concentration in fresh media and assumed that the culture starts from $n(t=0) = 10^{-7}$. The metabolite consumption rate α was then adjusted such that the culture reached saturation (i.e.

f reaches f_{crit}) when the OD is of order 1 (because of exponential growth, the value of f_{crit} itself only has a weak influence as long as f_{crit} is significantly smaller than f_0).

In the context of the microfluidic trap, cells are densely packed, such that, in the same dimensionless units, n_{trap} (the constant density assumed throughout the trap) should be of order 1. To account for the rod shape of the cells and non-optimal packing, we chose a value of $n_{trap} = 1/3$. Diffusion coefficients of metabolites in aqueous solutions range between 500 and 2000 $\mu m^2 s^{-1}$,[†] including potentially relevant aminoacids[5]. In light of the crowded environment in the trap, we chose a value at the lower end of this range, $D_f = 500\,\mu m^2 s^{-1}$, consistent with a recent study on biofilm front propagation[6]. Without further adjustments, the combination of diffusion, cell density and metabolite consumption rates (from the batch culture setting) indeed caused the metabolite concentration to reach f_{crit} within the boundaries of a $L = 170\,\mu m$-deep traps (Extended Data Fig. 5d) leading to a growth pattern that closely resembles the experimental observation. We therefore concluded that the physical scales of our two modeling settings were consistent.

It is interesting to note that the parameters α, α_0 and D_f are in a regime where the time scale of Eq. (14c) is sufficiently short for the diffusion process to essentially become a quasi steady state: At any given time point, the profile of f is very close to the steady state of Eq. (14c), and, therefore, increasing all three parameters further by a common factor does not alter model dynamics. Effects only start being noticed when these parameters are reduced by about two orders of magnitude. Thus, while diffusion provides the feedback for the oscillator circuit (Fig. 2c), it does not cause

[†] see Ref. 4, pp. 32, Table 2.1

any significant delay by itself, as communication through diffusion is virtually instantaneous.

Other rates were chosen to closely match experimental observations for the sensor and actuator components. Note that β simply scales p, and p's effect on growth rate, Eq. (4), is unaltered if p_{crit} is adjusted accordingly, so only the ratio β/p_{crit} (or IPTG$/p_{crit}$ for externally induced GRP) is a real model parameter.

The following table lists the parameters used for all numerical simulations in this study. Concentrations are dimensionless.

parameter	value
L	$170\,\mu m$
D_f	$18 \times 10^5\,\mu m^2 h^{-1} = 500\,\mu m^2 s^{-1}$
n_{trap}	1/3
f_0	1
g_0	$2.5 \cdot \log(2)\,h^{-1}$
α	$600\,h^{-1}$
α_0	$120\,h^{-1}$
f_{crit}	0.2
F_1	75
F_2	50
δ	0.01
σ	0.002
β	$\beta_{\text{metabolic}} + \text{NaCl} = 0.6\,h^{-1} + \text{NaCl}$
p_{crit}	0.4
γ_p	$1\,h^{-1}$
γ_c	$0.3\,h^{-1}$

Initial conditions at $t = 0$ were $f = f_0$ (also used as the Dirichlet boundary condition at $x = 0$ in the spatial case), $p = 0$ and $c = g_0/(\gamma_c + g_0)$. In batch culture, we assumed an initial cell density (vol/vol) of $n = 10^{-7}$ (i.e. roughly OD 0.0001). As described in the previous section, in the

spatiotemporal model, we assume a constant cell density throughout the trap of $n = n_{trap} = 1/3$.

Simplifying modeling assumptions

The interplay of metabolism, growth and nutrient diffusion is a very complex process whose accurate quantitative description would require a myriad of dynamical variables and equations. However, in order to have a tractable (but still relevant) semi-quantitative model and simplify interpretation of the modeling results, we made a number of simplifying assumptions. In particular, Eq. (4) models growth rate as an algebraic (instantaneous) function of the concentration of the limiting nutrient in order to keep the total number of dynamic variables low. This is an idealization, since in reality intracellular processes involving intermediate metabolic reactions and active growth rate regulation lead to a gradual adaptation of the growth rate to current extracellular conditions, which would have to be modeled by its own set of differential equations. One consequence of such idealization is that, in our model, bulk OD curves (representing plate reader experiments) exhibit a sharp transition from exponential to stationary phase (Extended Data Fig. 5a), while the experiment (as seen in the plate reader OD curves, e.g., Fig. 1e) shows a more gradual transition, as the adaptation takes place *in time*. In contrast, microfluidic trap experiments show the sharp *spatial* boundary between the different growth states, as the experimental system has time to adapt when the different growth states coexist *in space*. We also checked that the predictions of our spatio-temporal model are robust with respect to this simplifying assumption. For example, modeling the growth rate by $\dot{g} = \gamma_g[G(f,p) - g]$ (with G as in Eq. (4) and $\gamma_g = 1\,\mathrm{h}^{-1}$) smooths the transition to stationary phase in simulated bulk OD curves, while giving a sharp growth-state transition in the spatially extended

system. This modified model still produces the oscillations of the sensor-actuator circuit.

As for the above-mentioned changes in growth rate, we also assumed simple algebraic dependencies of protein expression rates on the nutrient level or growth state, together with a simplified single-step, deterministic protein production process. For expression of GRP from the IPTG-inducible promoter, Eq. (7), these simplifications lead to biphasic bulk behavior of GRP levels (Extended Data Fig. 5b). In reality, stochastic transcription/translation and fluorophore maturation cause significant smoothing of the fluorescence curve as seen in the experimental data. In addition, prescribing a smooth dependence of the pLlacO-1 expression rate on the growth state and assuming a more gradual growth rate adaptation as discussed above would help to avoid this modeling artifact. However, in the absence of information on the necessary dependencies, tuning the model in this way would unnecessarily sacrifice conceptual simplicity without providing additional insight, so we decided to keep the simpler version. This is true in particular since the characteristics of the IPTG promoter do not play a part in the oscillations, where GRP is expressed from pOsmY instead.

The observant reader might also notice that, in plate reader experiments (Fig. 1e), NaCl itself seems to induces a small difference in growth behavior. However, given the high osmolarity required and the robustness of the spatial growth pattern with respect to changes in osmolarity (Extended Data Fig. 3b), we concluded that this effect can be safely neglected for our qualitative modeling.

1. Scott, S. R. *et al.* A stabilized microbial ecosystem of self-limiting bacteria using synthetic quorum-regulated lysis. *Nature Microbiology* **2**, 17083 (2017).

2. Lies, M. & Maurizi, M. R. Turnover of Endogenous SsrA-tagged Proteins Mediated by ATP-dependent Proteases in Escherichia coli. *The Journal of Biological Chemistry* **283**, 22918 (2008).

3. Sezonov, G., Joseleau-Petit, D. & D'Ari, R. Escherichia coli physiology in Luria-Bertani broth. *Journal of Bacteriology* **189**, 8746 (2007).

4. Stein, W. D. *Channels, Carriers, and Pumps*. An Introduction to Membrane Transport (Academic Press, 1990).

5. Ma, Y., Zhu, C., Ma, P. & Yu, K. T. Studies on the Diffusion Coefficients of Amino Acids in Aqueous Solutions. *Journal of Chemical & Engineering Data* **50**, 1192 (2005).

6. Wang, X., Stone, H. A. & Golestanian, R. Shape of the growing front of biofilms. *New Journal of Physics* **19**, 125007 (2017).

7. Prindle, A. *et al.* A sensing array of radically coupled genetic 'biopixels'. *Nature* **481**, 39 (2012).

8. Andersen, J. B. *et al.* New Unstable Variants of Green Fluorescent Protein for Studies of Transient Gene Expression in Bacteria. *Applied and Environmental Microbiology* **64**, 2240 (1998).

Supplementary tables and figures

Strain	Plasmids	Figs.	Extended Data Figs. (Supp. Figs. if noted)
PB01	p15A-pLux-mKate2 (Cm)	1b, 1c	1, 2
PB02	pColE1-pOsmY-GFP-LAA (Amp) p15A-pLux-mKate2 (Cm)	1f, 1e	3a,b, 6
PB02a	pColE1-pOsmY(LAA)-GFP-LAA (Amp) p15A-pLux-mKate2 (Cm)		6
PB03	p15A-pLlacO1-mCherry (Cm)	1g	
PB04	p15A-pLux-mCherry-AAV (Cm)	1h, 3c, 3d, 3f	8
PB05	pColE1-pLlacO1-GRP-LAA (Kan)	2a, 2b	4
PB06	pColE1-pOsmY-GRP-LAA (Amp) p15A-pLux-mKate2 (Cm)	2f, 2g, 2h	3c, 6
PB06a	pColE1-pOsmY-GRP (Amp) p15A-pLux-mKate2 (Cm)		6
PB07	p15A-pLux-X174E-AAV (Cm)	3e-h	7
PB08	p**Gate**-ColE1-pOsmY-luxR (Amp) p15A-noLuxR-pLux-mCherry-AAV (Cm)	3c, 3d, 3f	8
PB09	p15A-noLuxR-pLux-mCherry (Cm)		Supp. Fig. 3
PB10	pColE1-pLlacO1-luxR (Kan) p15A-noLuxR-pLux-mCherry (Cm)		Supp. Fig. 3
PB10a	pColE1-pLlacO1-mCherry (Kan)		Supp. Fig. 3
PB11	p15A-pLux-mCherry (Cm)		Supp. Fig. 3
PB12	p**Gate**-ColE1-pOsmY-luxR (Amp) p15A-noLuxR-pLux-mCherry (Cm)		Supp. Fig. 3
PB13	p**Gate**-ColE1-pOsmY-luxR (Amp) p15A-noLuxR-pLux-X174E-AAV (Cm)	3e-h, 4	10

Supplementary Table 1 List of the strains used in this study. Strains are ordered by their first appearance, along with the contained plasmids, selection antibiotics (ampicillin: Amp, chloramphenicol: Cm, kanamycin: Kan) and references to figures containing experimental data obtained from them.

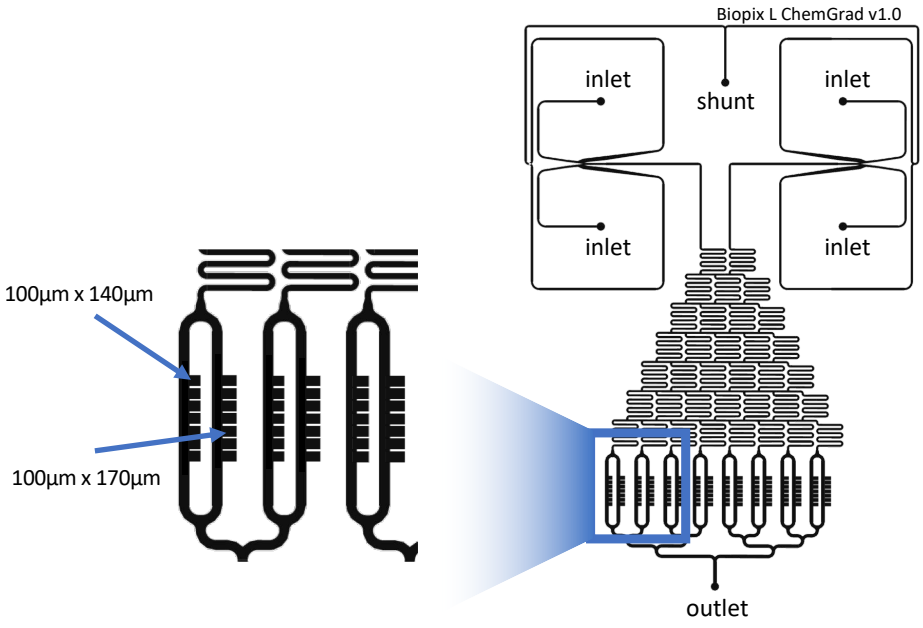

Supplementary Figure 1 Microfluidic device used in this study. The device features 4 inlets, a shunt preventing backflow into inlet ports by receiving currently unused media, and an outlet. Inlet hydrostatic pressure can be varied by changing media reservoir heights to select the top or bottom inlet on either side of the chip. For time-dependent induction experiments, typically, only the shunt, one port on the left side, two ports on the right side and the outlet were punched to create the sockets for plugging in reservoir connections. The three inlet ports are fed from reservoirs containing the growth media, where one reservoir on the right side additionally contains the inducer. A linear mixer creates 8 different mixtures – from 100% left growth medium to 100% right growth medium – which are each fed into two channels, to which the cell traps are attached (two different depths, 7 traps each: $100\mu\mathrm{m} \times 140\mu\mathrm{m}$ and $100\mu\mathrm{m} \times 170\mu\mathrm{m}$). The height (distance from glass cover slip to PDMS ceiling) is 1.6 to $1.8\mu\mathrm{m}$ within the cell traps and $40\mu\mathrm{m}$ for the channels, similar to the "biopixels" design used in previous studies from our group[7]. Media at different inlets contain different amounts of fluorescent dye to retrospectively determine the inducer concentration from microscopy images (see Supp. Fig. 2).

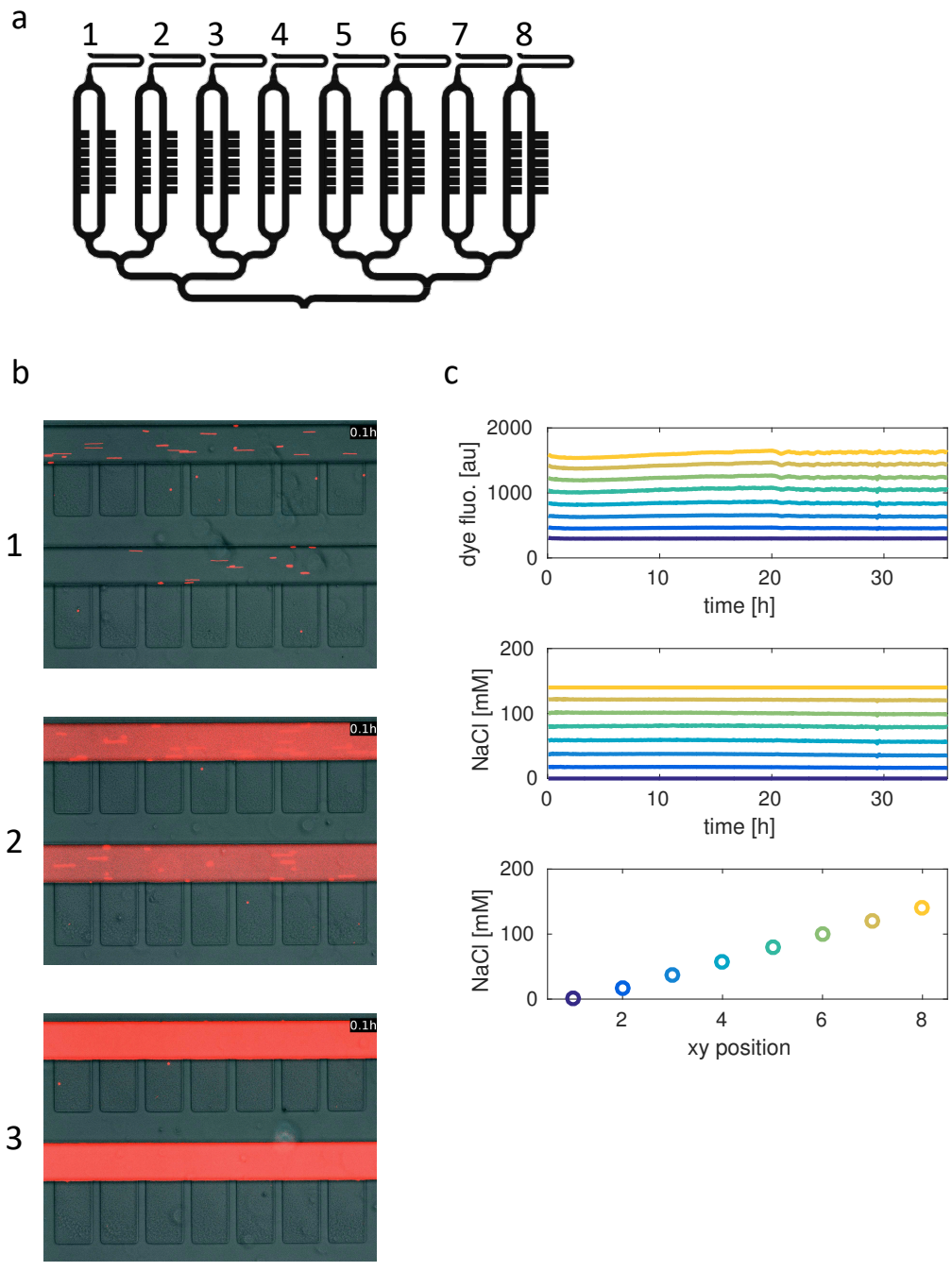

Supplementary Figure 2 On-chip mixing of two different growth media. **a**, Trapping region of the microfluidic chips with numbered media supply channels containing different media mixtures. **b**, Example microscopy images of trapping regions connected to media supply channels 1, 2 and 3. One of the two media fed into the mixer contains a red fluorescent dye, leading to distinct fluorescence intensities in the different channels. The small streaks also visible in the images are fluorescent beads used to determine

flow rate. **c**, (*Top*) Averaged raw fluorescence signal measured over time in each of the 8 imaging positions (i.e. channel regions with different media). Colors indicate channel number from blue (position 1) to yellow (position 8). (*Middle*) Raw fluorescence values are then normalized by minimum and maximum fluorescence at each time point. Assuming that the highest fluorescence corresponds to 100% of media *with* dye and the lowest fluorescence corresponds to 100% media *without* dye, differential media composition is calculated for each position by linear scaling between these min and max values at each time point (in this case, the media with dye contained 140mM NaCl). The purity of media in the two channels yielding min and max fluorescence is verified throughout each experiment by imaging additional positions upstream of the trapping region. (*Bottom*) Average calculated chemical composition at each position over the entire time of the experiment.

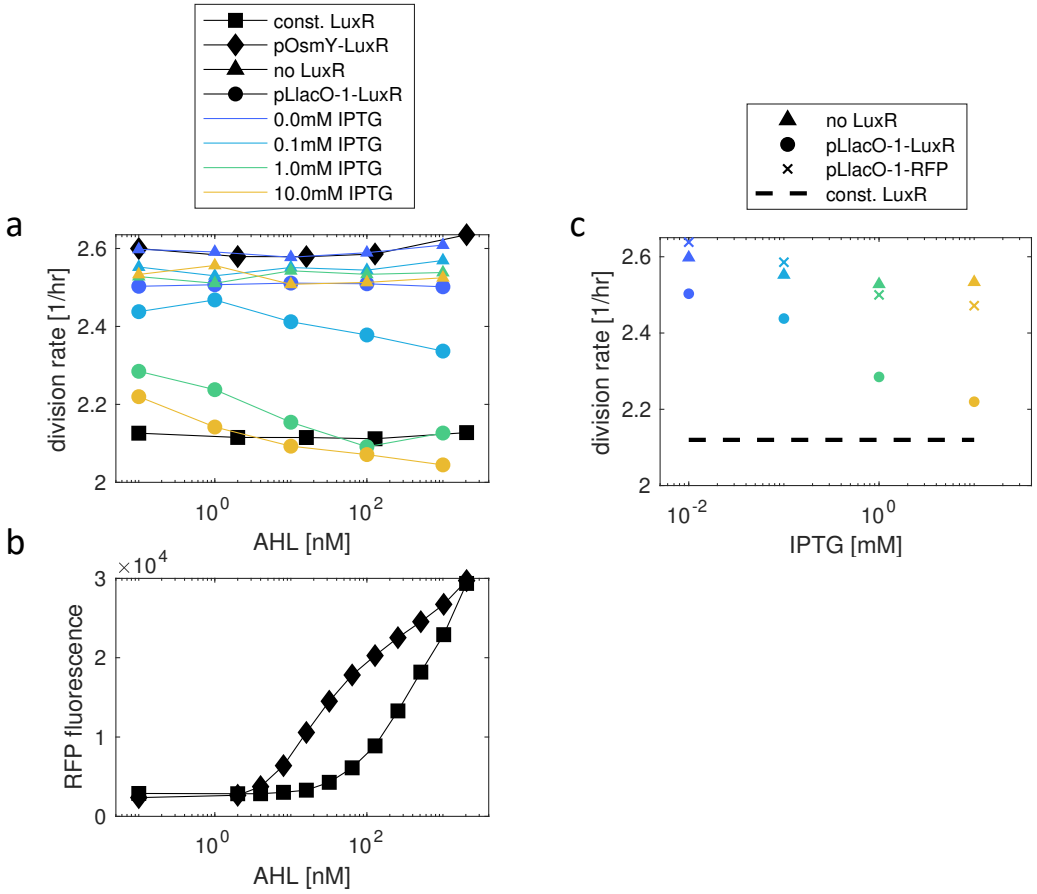

Supplementary Figure 3 Expression of LuxR impacts growth rate during exponential growth. a, We compared growth rates in the plate reader between OD 0.08 and 0.2 for cells expressing untagged RFP from the AHL-inducible pLuxI promoter. 4 different strains were tested that differed in their expression of the LuxR regulator protein: (1) constitutive LuxR from the traditional bidirectional LuxR-pLuxR-pLuxI cassette; (2) pOsmY-driven LuxR as in our gating circuit (Fig. 3a, where target gene = RFP-ssrA); (3) no LuxR at all; (4) LuxR expressed from the IPTG-inducible pLlacO-1 promoter. The constitutive and the gating circuit show consistently low and high growth rates, respectively, across all AHL concentrations. The pLlacO-1-LuxR construct approaches the same low growth rates upon induction with IPTG, whereas the no-LuxR control shows no such effect, suggesting that it is indeed LuxR that causes slowed growth. **b**, Peak RFP fluorescence of the constitutive-LuxR circuit and and the gating circuit from panel a. Expression from the gating circuit is significantly increased for lower concentrations of AHL, indicating sufficient expression of LuxR at later growth phases. **c**, Comparison of growth rates with an additional control strain pLlacO-1-RFP, where LuxR was replaced with RFP in the pLlacO-1-LuxR construct. Only the pLlacO-1-LuxR construct

itself shows a growth rate reduction comparable to constitutive LuxR expression (dashed line, obtained from the 0nM AHL data point in panel a), showing that transcription/translation cost from this plasmid/promoter combination is unlikely to be the cause of the reduced growth rate.

Supplementary Figure 4 Maps of all plasmids used in this study. "ssrA" in annotations and "LAA" in plasmid names both refer to the strong ClpXP-specific ssrA degradation tag with amino-acid sequence "AANDENYALAA". "ssrA-AAV" and "AAV" refer to the weaker degradation tag "AANDENYAAAV"[8]. For

details regarding assembly and strains, see Methods. Note that, for conciseness, the additional control constructs in Extended Data Fig. 6c and 3c are not depicted here. In the first case, an ssrA-LAA tag was inserted directly before the stop codon at the end of pOsmY in pColE1-pOsmY-GFP-LAA (resulting in pColE1-pOsmY(LAA)-GFP-LAA) and the ssrA-LAA tag was removed from GRP in pColE1-pOsmY-GRP-LAA (resulting in pColE1-pOsmY-GRP). In the second case, the luxR gene was replaced by mCherry in the pColE1-pLlacO1-luxR construct, resulting in pColE1-pLlacO1-mCherry. For annotaded nucleotide sequences of these plasmids, see Supplementary Data.